EFFECT OF PORE ARCHITECTURE OF 3D PRINTED OPEN POROSITY CELLULAR STRUCTURES ON THEIR RESISTANCE TO MECHANICAL LOADING: PART II – NUMERICAL ANALYSIS

Mehmet ALADAG*

Monika BERNACKA*

Adrian DUBICKI*

Izabela ZGŁOBICKA*

*Faculty of Mechanical Engineering, Bialystok University of Technology, Wiejska 45C, 15-351 Bialystok, Poland
**Technology Applied Sp. z o.o., Wiejska 42/3, 15-509 Sobolewo, Poland

mehmet.aladag@sd.pb.edu.pl, monika.bernacka@sd.pb.edu.pl, a.dubicki@pb.edu.pl, i.zqlobicka@pb.edu.pl

received 15 June 2023, revised 15 November, accepted 17 November

Abstract: The objective of this study was to investigate pore shape effect on resistance to compression of open porosity lattice structures obtained with 3D printing. To this end, three distinct pore architectures were investigated: ellipsoidal, helical and X-shape. Open porosity of these structures was 54%, 50% and 60%, respectively. Their mechanical properties were evaluated through compression tests, and their behaviours were analysed using finite element modelling (FEM). The results indicated that the pore size has a significant effect on the stiffness of cellular structures. It was observed that the helical structure exhibited superior properties among the structures tested due to homogenous stress distribution. It was also found that ellipsoidal and x-shape structures are much more sensitive to localisation of the deformation.

Key words: lattice structures, symmetry, 3D printing, porous elements, compression, finite element method

1. INTRODUCTION

The recent development of 3D printing methods has opened new opportunities for the fabrication of open porosity lattice structures (OPLSs). Such structures generally are characterised by a low weight and find applications in a number of products ranging from tissue engineering to motor parts (1).

Generally, the strength of OPLSs depends on the properties of printing materials and total porosity (2). Architected porous materials, developed to meet strength, stiffness, and toughness needs, offer improved mechanical properties, saving on weight and costs without compromising structural integrity in various engineering domains (3). However, as it is already common knowledge for composite materials, OPLSs can be viewed as pore-interpenetrated composites; also size, shape and spatial arrangement of pores influence their mechanical properties. Thirunavukkarasu et al. (4) demonstrated that manipulating topology unit cell designs with consistent aspect ratios can enhance mechanical performance, resulting in increased critical load tolerance, optimised buckling resistance and improved energy dissipation rates for versatile applications. The influence of pore size/shape/distribution, in short, pore architecture, can be analysed directly by considering the size/shape connectivity of struts, which are counterparts to pores in OPLSs. Indirectly, the strength of OPLSs can be approached with stereological parameters such as the volume fraction of pores, Vv. and their specific surface Sv (5). Both approaches are adopted in the present study to infer the effect of pore shape on the mechanical properties of OPLSs.

Analysis of the effect of pore architecture on properties of OPLSs presented here is stimulated by results recently reported by Bernacka et al. (6). In part one, five different lattice structures

with various pore sizes and shapes, with two volume fractions for each, and shapes (ellipsoidal, helical, X-shape, trapezoidal and triangular) were designed and fabricated using the selective laser sintering (SLS) additive manufacturing (AM) method. Mechanical properties were tested through uniaxial compression, and the apparent stress-strain curves were analysed. In part two, we selected three lattice structures, ellipsoidal, helical and X-shape, that show outstanding compressive strength properties in the compression test. From this end, we include in the analysis as reference structures the ones discussed in Ref. (7) and take into account the results presented in Refs (8–10). Mechanical properties we analyse using finite element analysis (FEA) are presented in Ref. (11–15).

2. EXPERIMENTAL MODELING

In order to investigate the effect of pore size on the properties of OPLSs, we studied the properties of three structures with porosity in the range of 50%–60%, as shown in Fig. 1. These structures have been printed by the SLS method with polyamide (PA-2200) polymer and tested in compression tests. Results of the compression tests have been analysed by finite element modelling (FEM), which is nearly routinely used in analyses of mechanical properties of OPLSs – see for example Refs (15–31).

The SLS method used here for printing OPLSs is one of AM technologies (33,34) Its distinct characteristic is that particles of powdered substrate are sintered by a laser beam with no formation of liquid phase. This allows for the fabrication of uniform structures of highly complex architecture. Ultra-light weight elements can be printed of controlled porosity by SLS, which is of

Mehmet Aladag, Monika Bernacka, Adrian Dubicki, Izabela Zglobicka

Effect of Pore Architecture of 3d Printed Open Porosity Cellular Structures on Their Resistance to Mechanical Loading: Part II Numerical Analysis

prime importance for the investigations carried out in the present study.

2.1. Material

Polyamide (PA-2200), used in the present study, is one of the most commonly employed materials in SLS printing technology offered by EOS. This synthetic thermoplastic polymer has high biocompatibility, flexibility, hygroscopicity, good chemical resistance as well as high strength and hardness. Selected mechanical properties of PA 2200 are listed in Tab. 1.

Tab. 1. Selected mechanical properties of PA 2200 (35)

Mechanical properties	Value	Unit
Density	930	kg/m³
Tensile strength	48	MPa
Tensile modulus	1,650	MPa
Strain at break	18	%
Melting temperature (20°C/min)	176	°C
Shore D hardness	75	_
Powder size	60	μm

2.2. Stereological parameters of designed structures

Three 3D lattice structures with distinctly different shapes of pores and degree of symmetry have been designed using CAD software SolidWorks. The size of the porosities was 1.9 mm for each lattice. The geometry of the designed lattices is depicted in Fig. 1.

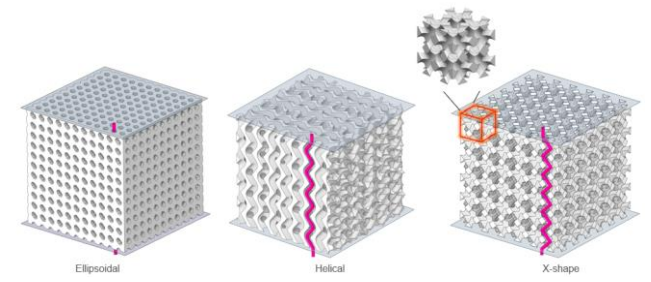


Fig. 1. Lattice structures investigated in this study and pore pathways along compression direction

Based on the shape of pores, one can be describe the structures presented in Fig. 1 as having cell units of:

- ellipsoidal,
- helical,
- X-shape.

Visually recognisable differences in the geometry of the three cell structures shown in Fig. 1 can quantified using principles of stereology – see for example Ref. (5). For cell structures like the ones analysed here, it is rational to focus attention on the pores, which account for more than 50% of their volume. Since pores are 3-dimensional features, their geometry can be quantified in terms of volume fraction, VV, size (e.g., equivalent diameter) and shape (using any of shape factors described in the literature). It should

be noted, however, that unlike in the case of close pores, size of pores in OPLSs from stereological point of view is an ill-defined parameter. This is because in OPLS there is one pore percolating throughout the structure of interest, and geometrical dimension of such pores depends on the size of structure. In this situation, pore surface to pore volume, SV, is used, the value of which does not depend on the physical dimensions of the open porosity structure of interest. It does not depend on the size of the structure. Its value increases with the decreasing distance in between the struts forming the lattice structure.

Stereological considerations show that parameter SV has can also be used to calculate a mean intercept length of porosity, i.e. average length of randomly oriented and positioned secants drawn across porosity in a given structure, \bar{l} , using the following stereological relationship:

$$\bar{l} = 2/S_V$$

Regarding shape of open porosity pores, it can be described by tortuosity; it is defined as the ratio of actual flow path length to the straight distance between the ends of the flow path. Taking into account symmetry of the structures of interest, we defined tortuosity in the way as shown in Fig. 1, i.e., by the ratio of actual vertical channel length to edge length.

The designed lattice structures were printed into cubes of dimensions 30 mm \times 30 mm \times 30 mm with similar porosity. In the analyses of their resistance to compression, applied force and average stress were normalised by porosity to set a stage for extracting a possible pore size effect. Values of the above-described stereological parameters for the designed structures are listed in Tab. 2.

Tab. 2. Stereological parameters of designed lattice structures

Structure	Porosity [%]	S _v [1/mm]	$ar{l}$ [mm]	L/L ₀
Ellipsoidal	54	3.62	7.24	1
Helical	50	2.22	4.44	1.2
X-shape	60	2.44	4.88	1.4

It can be noted from Tab. 1 that all the structures differ in pores volume fraction, which is highest for X-Shape, pore size, which is lowest for helical structure and shape/tortuosity, which is highest for ellipsoidal.

2.3. Compression tests and FEM

Compression tests of the lattice structures were carried out using the SHIMADZU 322 MTS Load Unit with a deflection rate of 1 mm/min, and the video extensometer ARAMIS 3D 4M was used to investigate the deformation. The recorded data were implemented by GOM Correlate software. Compression force-displacement curves were normalised to compression stress-compression strain ones. To this end, applied force was divided by surface of cube (30 mm \times 30 mm) and induced displacement by cube edge length. Further experimental details can be found in a paper by M. Bernacka (6).

The compression behaviours of the printed lattice structures were analysed using Marc Mentat FEA software (36). Schematic explanation of modelling is given in Fig. 2. A tetrahedron element

DOI 10.2478/ama-2024-0047

type was utilised to generate the mesh of the lattice structures. The average number of elements was 250,000 for each structure. Compression of the structures was modelled by applying up to 20% reduction of height induced with rigid plates. FEM results were analysed in terms of macroscopic stress-strain relationships for three geometries of interest.



Fig. 2. Schematic explanation of: (a) compression test FEA model, (b) mesh view of each structures. FEA, finite element analysis

Nonlinear elastic-plastic properties evaluated of the printed structure were established through the curve a fitting method. The experimental results obtained in tensile tests of bulk coupled with PA 2200 as reported in Ref. (37). Results of this curve fitting exercise are shown in Fig. 3. A fully satisfactory agreement between experimental and modelled tensile curves was obtained, which rationalized the use of the numerical approximation of elastic-plastic properties obtained in further computations.

In FEA, we used 10 mm \times 10 mm \times 10 mm cells representative for lattice structures of interest. In modelling compression tests, these cells were placed between two rigid stamps.

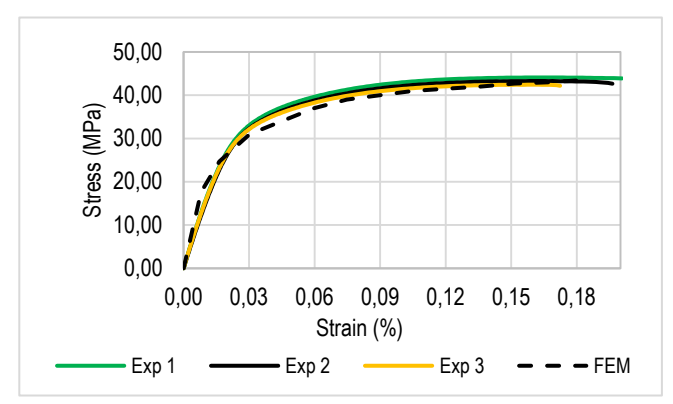


Fig. 3. Experimental and FEM tensile test curves. FEM, finite element modelling, Exp, experimental test

3. RESULTS

The stress-strain curves obtained in compression tests for the three structures investigated here are shown in Fig. 4 together with FEM modelling.

The results shown in Fig. 4 indicate that the helical lattice structure exhibits significantly higher resistance to compression than the other two structures. The compressive strength and stress were normalised by dividing the density of the lattice structure. Therefore, specific strength and specific stress were obtained (see Tab. 3). Based on the calculation, the helical structure has outstanding properties, in terms of specific stress 33,850 MPa/g/mm³ and specific strength 3,386 kN/g/mm³, compared with ellipsoidal and X-shape (see in Fig. 5).

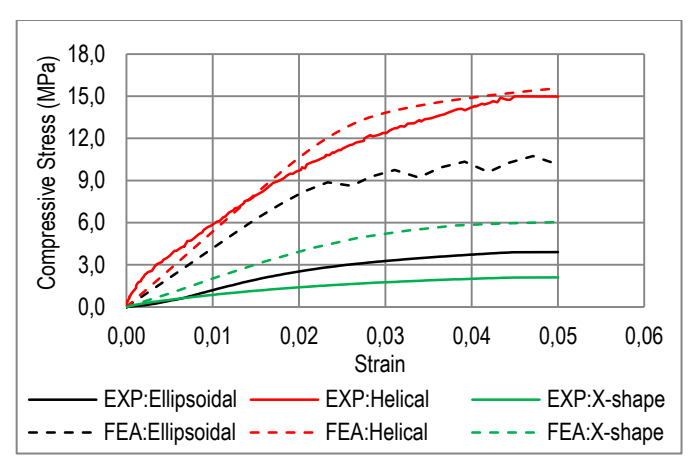
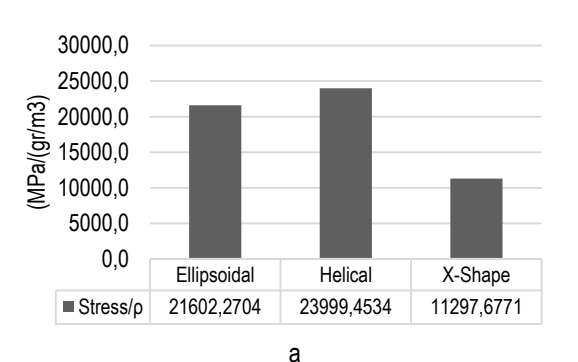


Fig. 4. Experimental compression stress-strain curves – solid lines, broken lines show results of FEA. FEA, finite element analysis and, EXP, experimental analysis

Tab. 3. Compressive stress, at 2% of deformation and volume of lattice structures

Structure property	Ellipsoidal	Helical	X-Shape
Volume (mm³)	408.161	495.531	390.222
Compressive stress at the strain 2% (MPa)	8.2	11.0	4.1
Compressive force at the strain 2% (kN)	0.8	1.1	0.4
Density of structures (gr/cm³)	0.38	0.46	0.36



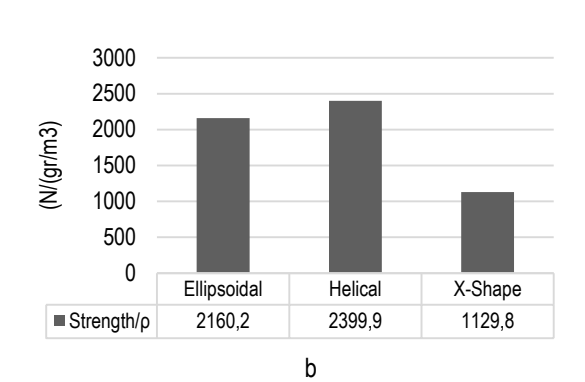


Fig. 5. (a) Specific stress and (b) specific strength of OPLSs.

Mehmet Aladag, Monika Bernacka, Adrian Dubicki, Izabela Zglobicka

Effect of Pore Architecture of 3d Printed Open Porosity Cellular Structures on Their Resistance to Mechanical Loading: Part II Numerical Analysis

An interesting observation can be made when analysing data in Fig. 4 that there is a major difference as far as agreement between the experimental values and the one obtained with FEM is concerned. FEM of compression of helical structure agrees well with experimental stress-strain curve. On the other hand, in the case of the other two structures, FEM grossly overestimated experimentally measured compression stress. Since FEM is an established tool for modelling deformation of composite materials, we consider the disagreement of numerical and experimental data for two OPLSs studied here as having background in physical properties and not as numerical error. In the following section, we provide explanation of these disparities.

4. DISSCUSION

One can discuss results presented here in terms of a relationship between stereological parameters of the investigated structures and their resistance to compression. Although with three structures differing in volume fraction, size and shape of pores, it is not possible to precisely determine character and parameters of the relationship governing their properties; there is a clear indication of the effect of pore size on the compression test. As can be noted, the ellipsoidal structure with the largest size of pores shows the lowest resistance to the compression stress.

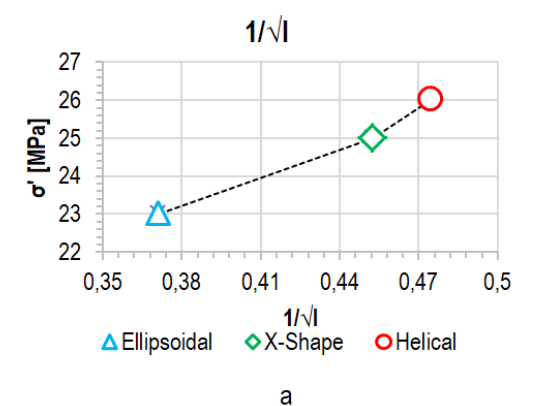
To elucidate the effect of pore size on compression of the structures of interest, normalized compression stress for 20% deformation (σ ') is plotted in Fig. 6 against $1/\sqrt{l}$, Fig. 6a, and 1/l Fig. 6b. These two plots are expected to linearise relationship between l and compression stress under two possible approaches. First, one can expect flow stress – size of pore relationship – as predicted by Hall-Petch who derived dependence of flow stress on the size of grains in metals. The other possible approach is based on mechanics of composites, under assumption that the struts of cellular structures can be as consisting of near surface layer of some physically defined thickness and the core. If this is the case, $1/\overline{l} = SV$ and determines the relative content of near surface zone.

It can be noted from the plot in Fig. 6 that both model relationships give reasonable agreement with experimental data. Obviously, with only three data points, it is difficult to draw conclusions; however, we suggest that the composite approach as shown in Fig. 6b gives a better agreement.

In the further discussion of the results presented in Fig. 4, we concentrate attention on two issues: (1) experimentally measured lower compression stress of elliptical and X-shape structures and (2) disparity between experimental and numerical results.

To explain differences in resistance to compression and the reasons for disagreement between experimental and modelled response to compression in the case of elliptical and X-shape OPLSs, we have analysed stress and strain distributions in the OPLS of interest and re-visited experimental detail of their compression tests.

Stress and strain distributions in the ellipsoid, helical and X-shaped structures computed with finite element method are shown in Fig. 7 and 8, respectively, for strain of 20%, (a reduction in height of the compressed cube). In analysing both stress and strain, we focused attention of homogeneity of their spatial distribution over the struts forming lattice structures.



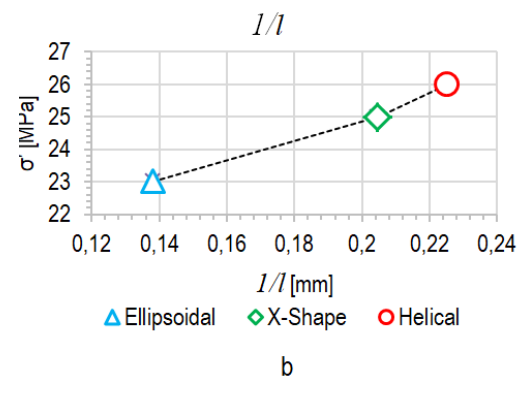


Fig. 6. Normalised stress with respect to average intercept length of porosity: (a) $1/\sqrt{l}$ and (b) $1/\overline{l}$

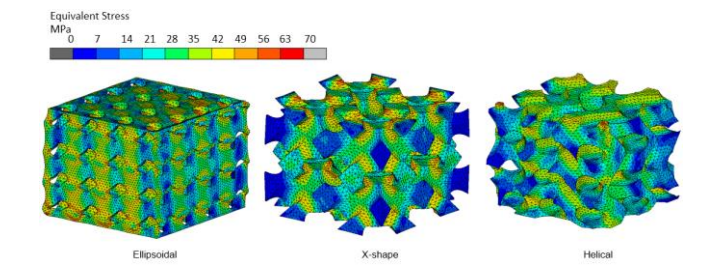


Fig. 7. Equivalent stress distributions for 20% of deformation

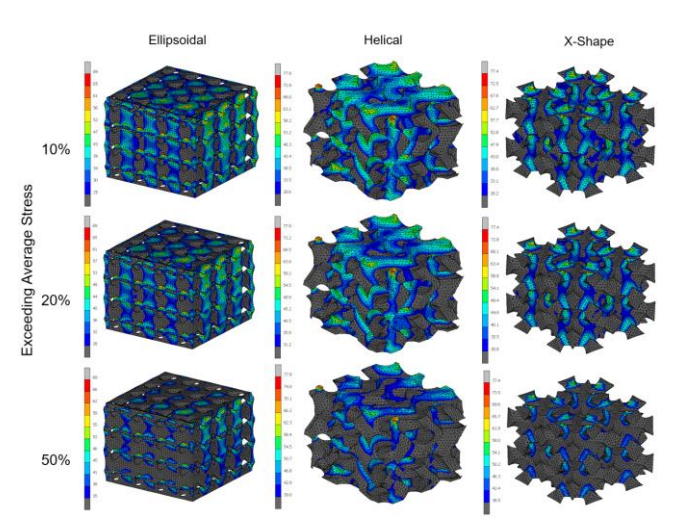


Fig. 8. Stress distribution by the value of equivalent stress exceeding the average equivalent by 10%, 20% and 50%

DOI 10.2478/ama-2024-0047

Graphical illustration (mapping) of equivalent stresses shown in Fig. 7 allows us to conclude that in the case of helical structures, stresses generated by compression are more uniformly distributed over the polymeric material forming the respective lattices. Helical type of cells increased the absolute stiffness and strength against the applied load (). One should also note that the stress concentrations are particularly high in the part of the structures in direct contact with load applying rigid stamps (see in Fig. 7).

In Fig. 8, the equivalent stress distribution on the OPLSs exceeding by 10%, 20% and 50% values of average stress and volume of the lattice elements carrying stress exceeding average value were calculated accordingly. The grey regions remained below the threshold stress values, and these regions were not included in the volume calculation.

These qualitative observations can be quantified by providing relative volume of the material with equivalent stress, exceeding the average equivalent stress by 10%, 20% and 50% values which are also listed in Fig. 9.

Based on the calculation of the volume that has the range of specified stress percentage, the concentrated stress per volume was plotted in Fig. 9. As can be seen from the data in the figure, elliptical and X-shape structures are characterised by significantly lower load carrying contribution of various parts of the structures.

The results of FEM of equivalent strain distribution are shown in Fig. 10. Generally, the same conclusions can be drawn with regard to load distribution over the materials of OPLSs analysed here. Visibly, strains are less uniform in ellipsoidal and X-shape structures, both in terms of inter-pore "bridges" being more strained and strain concentrations in the near-stamp zone.

Fig. 10 shows also images captured by Aramis video extensometer system during compression tests. These are images recorded for side-walls. As a result, in the case of elliptical structure, pores are clearly visible, unlike in the case the helical and X-shape ones. Thus, it was possible to investigate shape of some of the pores, e.g. the two indicated with arrows in the lower row in Fig. 10. One can clearly see that the pore next to the upper stamp

is much more elongated (deformed) in comparison with the other one. An important conclusion can be drawn that plastic deformation in elliptical structure is non-uniform and higher in the near-stamp zone. Other ARAMIS images confirm that the same applies to X-shape one, while in the case of helical structure, no localisation in near-surface zone was observed. This uniformity of strain distribution in the helical structure against strain localisation near to the compressed surface in the other two is the reason for the disparity between FEM modelling and experimental stress-strain curves shown in Fig. 4.

In explaining the disparity between experimental stress-strain curves and the ones obtained numerically, it should be noted that, experimental results obtained with ARAMIS indicate much higher strain localisation than estimated from FEM modelling. Thus, it concluded that within modelling carried out in the present paper, we can provide rational for propensity of elliptical and X-shape structures to strain localisation in the near to the compression stamp zone. However, we were not able fully capture in our models strain localization intensity.

FEM modelling was also used to discern details of stress distributions in the respective lattice structures under compression. The results presented in Fig. 11 and 12 concern stress vectors and flow lines, respectively. The stress vector distributions in Fig. 11 reveal that in the case of ellipsoidal and X-shaped structures, the stress vectors form a less regular pattern compared to that of the helical structure. Specifically, in the ellipsoidal structure, the stress vectors are concentrated in vertically oriented struts, leading to their buckling. In contrast, in the helical structure, the stress vectors are concentrated in horizontally oriented struts, with the concentration being perpendicular to the applied load. As a result of the pore shape in this structure, it can be noted that significant distortion or buckling-induced deformation does not occur, and stress concentrations are also minimised. In the X-shaped structure, the vectors are primarily perpendicular to the outer surface, with the highest concentration of stress vectors occurring at the point of highest strain, as seen in Fig. 11.

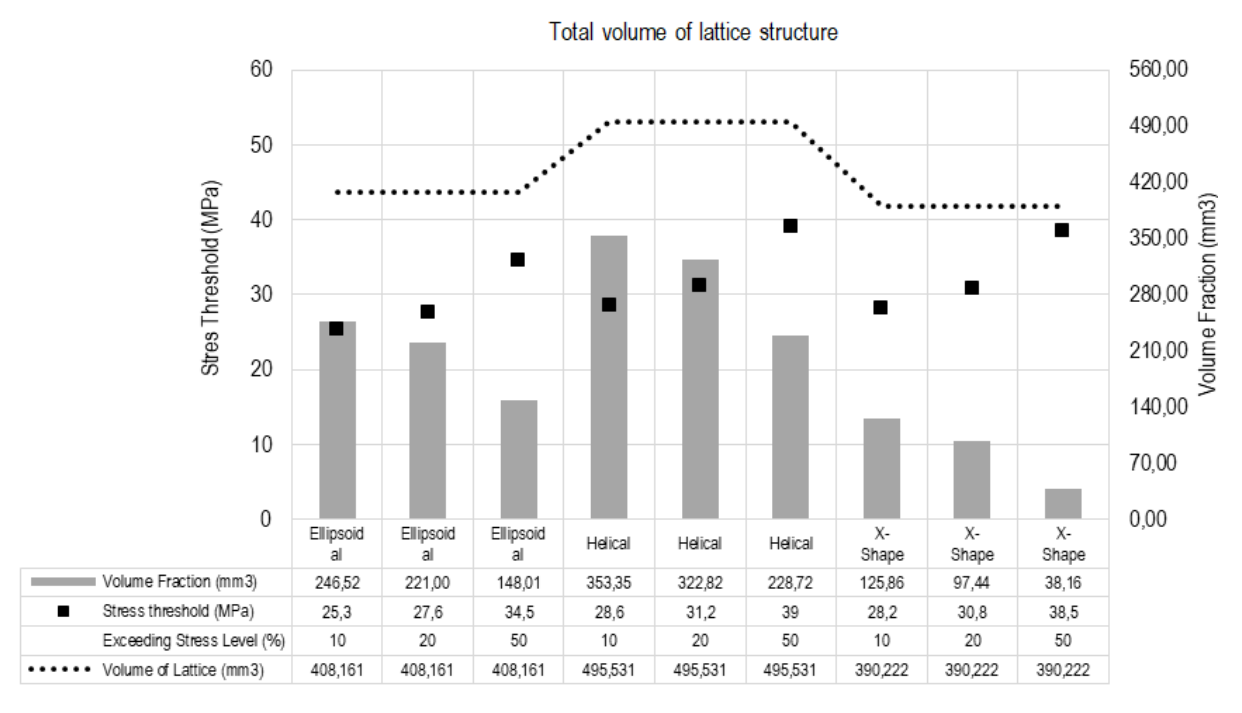


Fig. 9. The exceeding stress (exceeding average equivalent stress by 10%, 20% and 50%) per volume fraction

Mehmet Aladag, Monika Bernacka, Adrian Dubicki, Izabela Zglobicka

Effect of Pore Architecture of 3d Printed Open Porosity Cellular Structures on Their Resistance to Mechanical Loading: Part II Numerical Analysis

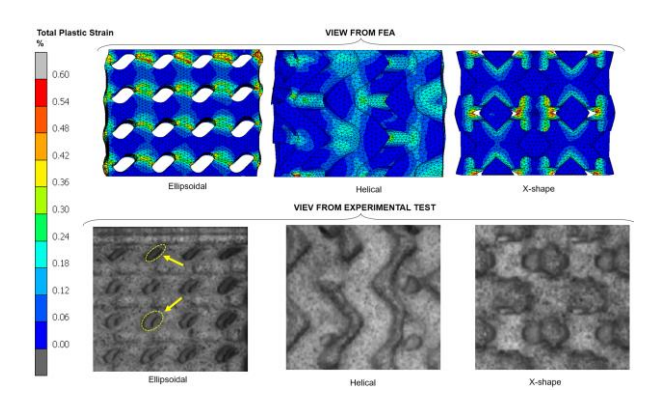


Fig. 10. Plastic strains distribution for 20% compression

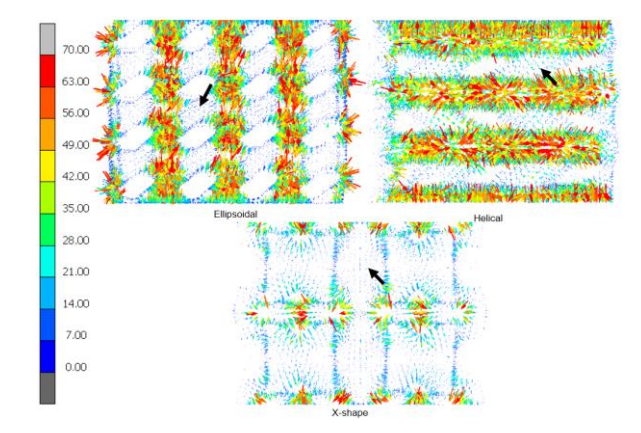


Fig. 11. Stress vectors, their direction and magnitudes of the structures

The material deformation flow patterns, depicted in Fig. 12, reveal that flow lines in helical and X-shape geometries are predominantly vertical, running from the top to the bottom of the structure. In the case of ellipsoidal structure, a distinct flow pattern is formed, with the pores altering the flow direction during loading. This deviation in the flow pattern may result in inhomogeneous deformation across the structure and may also lead to a change in the direction of loading, resulting in unsymmetrical deformation and a decrease in stiffness.

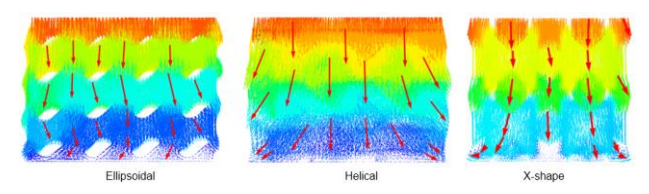


Fig. 12. Material flowlines during deformation

Results presented in Fig. 12 show similarity in flowline patterns in helical and X-shape structures. However, other analyses clearly indicate that X-shape differs from helical structures in terms of stress/strain and stress vector distribution.

5. CONCLUSIONS

The results obtained can be concluded in the following points, which are categorised into one based on stereological and micromechanical considerations.

Within the stereological approach to predicting properties of OPLSs, it has been demonstrated that:

- pore size has an important effect on compression stress of OPLSs
- outstanding stiffness of helical structures can also be attributed to the shape of pores

Within the micromechanics approach, the outstanding stiffness of helical OPLSs stems from much more uniform stress and strain distribution over the material of struts forming the respective structures. One may also note that in helical structures, stress vectors are well aligned and predominantly normal to the compression axis; hence, the presence of a helical structure amplified the overall stiffness and strength in response to applied loads.

An attempt to explain the disagreement between results of FEM modelling and experimental data brought attention to the phenomenon of strain localisation in the zone near to compression stamp, in fact captured with Aramis video extensometer system for monitoring progress in deformation in compression tests. Susceptibility of OPLS structure to localisation of strain is subject of a separate paper.

Results of the present study highlight importance of pore shape on the properties of high porosity structures. They also provide an insight into deformation of OPLSs and limitations in deformation modelling with FEM.

REFERENCES

- Korkmaz ME, Gupta MK, Robak G, Moj K, Krolczyk GM, Kuntoğlu M. Development of lattice structure with selective laser melting process: A state of the art on properties, future trends and challenges. J Manuf Process. 2022 Sep 1;81:1040–63.
- Tian L, Lu L, Chen W, Xia Y, Wang CCL, Wang W. Organic Opencell Porous Structure Modeling. In: Symposium on Computational Fabrication [Internet]. New York, NY, USA: ACM; 2020. p. 1–12. Available from: https://dl.acm.org/doi/10.1145/3424630.3425414
- Mora S, Pugno NM, Misseroni D. 3D printed architected lattice structures by material jetting. Mater Today [Internet]. 2022;59: 107–32. Available from: https://doi.org/10.1016/j.mattod.2022.05.008
- Thirunavukkarasu N, Gao J, Peng S, Laroui A, Wu L, Weng Z. Mechanically robust 3D printed elastomeric lattices inspired by strong and tough hierarchical structures. Addit Manuf [Internet]. 2023;66(November 2022):103451. Available from: https://doi.org/10.1016/j.addma.2023.103451
- Kurzydłowski KJ, Ralph B. The quantitative description of the microstructure of materials. CRC Press; 1995. 418 p.
- Bernacka M, Aladag M, Dubicki A, Zgłobicka I. Effect of Pore Architecture of 3d Printed Open Porosity Cellular Structures on their Resistance to Mechanical Loading: Part I – Experimental Studies. Acta Mech Autom. 2024;18(3):419–26.
- Montazerian H, Davoodi E, Asadi-Eydivand M, Kadkhodapour J, Solati-Hashjin M. Porous scaffold internal architecture design based on minimal surfaces: A compromise between permeability and elastic properties. Mater Des [Internet]. 2017 Jul;126(April):98–114. Available from: http://dx.doi.org/10.1016/j.matdes.2017.04.009
- 8. Li S, Yuan S, Zhu J, Zhang W, Tang Y, Wang C, et al. Optimal and adaptive lattice design considering process-induced material anisotropy and geometric inaccuracy for additive manufacturing. Struct Multidiscip Optim. 2022 Jan 1;65(1):1–16.
- Barbaros I, Yang Y, Safaei B, Yang Z, Qin Z, Asmael M. State-of-theart review of fabrication, application, and mechanical properties of functionally graded porous nanocomposite materials. Nanotechnol Rev [Internet]. 2022 Jan 1 [cited 2022 Oct 22];11(1):321–71. Available from: https://www.degruyter.com/document/doi/10.1515 /ntrev-2022-0017/html

DOI 10.2478/ama-2024-0047

- Liu R, Ma L, Liu H, Xu B, Feng C, He R. Effects of pore size on the mechanical and biological properties of stereolithographic 3D printed HAp bioceramic scaffold. Ceram Int. 2021 Oct 15;47(20):28924–31.
- Jiao C, Xie D, He Z, Liang H, Shen L, Yang Y, et al. Additive manufacturing of Bio-inspired ceramic bone Scaffolds: Structural Design, mechanical properties and biocompatibility. Mater Des. 2022 May 1;217.
- Cerardi A, Caneri M, Meneghello R, Concheri G, Ricotta M. Mechanical characterization of polyamide cellular structures fabricated using selective laser sintering technologies. Mater Des. 2013 Apr 1:46:910–5.
- Cipriani CE, Ha T, Martinez Defilló OB, Myneni M, Wang Y, Benjamin CC, et al. Structure–Processing–Property Relationships of 3D Printed Porous Polymeric Materials. ACS Mater Au [Internet]. 2021 Sep 8 [cited 2022 Oct 22];1(1):69–80. Available from: https://pubs.acs.org/doi/full/10.1021/acsmaterialsau.1c00017
- Zeleniakienė D, Kleveckas T, Liukaitis J, G. M. The Influence of Porosity on Stress and Strain State of Porous Polymer Materials. Mater Sci. 2003;9(4):358–62.
- Chen X, Ji Q, Wei J, Tan H, Yu J, Zhang P, et al. Light-weight shell-lattice metamaterials for mechanical shock absorption. Int J Mech Sci [Internet]. 2020;169(August 2019):105288. Available from: https://doi.org/10.1016/j.ijmecsci.2019.105288
- White DA, Kudo J, Swartz K, Tortorelli DA, Watts S. A reduced order model approach for finite element analysis of cellular structures. Finite Elem Anal Des [Internet]. 2023 Feb [cited 2022 Oct 26];214:103855. Available from: https://linkinghub.elsevier.com/retrieve/pii/S0168874X22001287
- Ni Y, Liao H, Zhao Q, Wu W, Shi Y, Wu S. Investigations of the failure behaviors of open-cell copper foam based on in-situ X-ray tomography compression experiments and image reconstructed finite element modeling. Eng Fract Mech. 2022 Mar 15;263:108323.
- Ruiz de Galarreta S, Jeffers JRT, Ghouse S. A validated finite element analysis procedure for porous structures. Mater Des. 2020 Apr 1;189.
- Abueidda DW, Elhebeary M, Shiang CS (Andrew), Pang S, Abu Al-Rub RK, Jasiuk IM. Mechanical properties of 3D printed polymeric Gyroid cellular structures: Experimental and finite element study. Mater Des. 2019 Mar 5;165:107597.
- Smith M, Guan Z, Cantwell WJ. Finite element modelling of the compressive response of lattice structures manufactured using the selective laser melting technique. Int J Mech Sci. 2013 Feb 1;67: 28–41.
- Zhong L, Li X. Simulation analysis of lightweight cylindrical lattice materials with different unit cells. J Coast Res. 2015 Mar; (73 (10073)):155–9.
- Sadeghzade M, Gharehbaghi H, Farrokhabadi A. Experimental and analytical studies of mechanical properties of additively manufactured lattice structure based on octagonal bipyramid cubic unit cell. Addit Manuf. 2021 Dec 1;48:102403.
- Chen W, Zheng X, Liu S. Finite-Element-Mesh Based Method for Modeling and Optimization of Lattice Structures for Additive Manufacturing. Mater 2018:23;11(11):2073.
- Song J, Wang Y, Zhou W, Fan R, Yu B, Lu Y, et al. Topology optimization-guided lattice composites and their mechanical characterizations. Compos Part B Eng. 2019 Mar 1;160:402–11.
- Leon-Patiño CA, Drew RAL. Role of metal interlayers in the infiltration of metal-ceramic composites. Curr Opin Solid State Mater Sci. 2005 Aug;9(4–5):211–8.
- Lim YE, Park JH, Park K. Automatic Design of 3D Conformal Lightweight Structures Based on a Tetrahedral Mesh. Int J Precis Eng Manuf Technol 2018 54 [Internet]. 2018 Aug 23 [cited 2022 Oct 26];5(4):499–506. Available from: https://link.springer.com/article/10.1007/s40684-018-0053-2
- Salonitis K, Chantzis D, Kappatos V. A hybrid finite element analysis and evolutionary computation method for the design of lightweight lattice components with optimized strut diameter. Int J Adv Manuf Technol 2016 909 [Internet]. 2016 Oct 21 [cited 2022 Oct 26];

- 90(9):2689–701. Available from: https://link.springer.com/article/10.1007/s00170-016-9528-x
- Yang L, Yan C, Cao W, Liu Z, Song B, Wen S, et al. Compression—compression fatigue behaviour of gyroid-type triply periodic minimal surface porous structures fabricated by selective laser melting. Acta Mater. 2019 Dec 1;181:49–66.
- Shin J, Kim S, Jeong D, Lee HG, Lee D, Lim JY, et al. Finite Element Analysis of Schwarz P Surface Pore Geometries for Tissue-Engineered Scaffolds. Math Probl Eng [Internet]. 2012;2012:1–13. Available from: http://www.hindawi.com/journals/mpe/2012/694194/
- Gonzalez FJQ, Nuno N. Finite element modeling of manufacturing irregularities of porous materials. Biomater Biomech Bioeng [Internet]. 2016 Mar 25;3(1):1–14. Available from: http://koreascience.or.kr/journal/view.jsp?kj=E1TPEG&py=2016&vnc=v3n1&sp=1
- Deliormanlı AM, Deliormanlı AH. Finite element method simulation for the prediction of mechanical properties of three-dimensional periodic bioactive glass scaffolds. J Aust Ceram Soc [Internet]. 2017 Oct 13;53(2):299–307. Available from: http://link.springer.com/10.1007/s41779-017-0037-7
- 32. Khrapov D, Koptyug A, Manabaev K, Léonard F, Mishurova T, Bruno G, et al. The impact of post manufacturing treatment of functionally graded Ti6Al4V scaffolds on their surface morphology and mechanical strength. J Mater Res Technol. 2020;9(2):1866–81.
- Gardan J. Additive manufacturing technologies: State of the art and trends [Internet]. Additive Manufacturing Handbook. CRC Press; 2017 [cited 2022 Oct 26]. Available from: https://www.taylorfrancis.com/chapters/edit/10.1201/9781315119106 -10/additive-manufacturing-technologies-julien-gardan
- Ngo TD, Kashani A, Imbalzano G, Nguyen KTQ, Hui D. Additive manufacturing (3D printing): A review of materials, methods, applications and challenges. Compos Part B Eng. 2018 Jun 15:143:172–96.
- PA 12 PA2200: Nylon for Industrial 3D Printing | EOS GmbH [Internet]. [cited 2022 Oct 10]. Available from: https://www.eos.info/en/additive-manufacturing/3d-printing-plastic/sls-polymer-materials/polyamide-pa-12-alumide
- MSC Software. Marc/Mentat 2020 Advanced Nonlinear FEA Software.
- Bernacka ME. Bio-inspired design and experimental verification properties of porous elements obtained by 3D printing. [Bialystok]: Bialystok University of Technology; 2021.
- Teng F, Sun Y, Guo S, Gao B, Yu G. Topological and Mechanical Properties of Different Lattice Structures Based on Additive Manufacturing. Micromachines. 2022;13(7).

The author would like to express their sincere gratitude to Professor Krzysztof J. Kurzydłowski for his invaluable supervision and guidance throughout this study. Additionally, the author extends their thanks to Technology Applied sp. z o. o for their generous support.

Mehmet Aladag: https://orcid.org/0000-0002-2484-7519

Monika Bernacka: https://orcid.org/0000-0003-3481-0768

Adrian Dubicki: https://orcid.org/0000-0002-3994-2957

Izabela Zglobicka: https://orcid.org/0000-0002-4432-9196



This work is licensed under the Creative Commons BY-NC-ND 4.0 license.